Comparative study of intersubband absorption in AlGaN/GaN and AlInN/GaN superlattices: Impact of material inhomogeneities

C. Edmunds,[1] L. Tang,[1,2] M. Cervantes,[1] M. Shirazi-HD,[2,3] J. Shao,[1,2] A. Grier,[4] A. Valavanis,[4] J. D. Cooper,[4] D. Li,[1,2] G. Gardner,[2,5] D. N. Zakharov,[6] Z. Ikonić,[4] D. Indjin,[4] P. Harrison,[4] M. J. Manfra,[1,2,3,5] and O. Malis[1,*]

[1]*Department of Physics, Purdue University, West Lafayette, Indiana 47907, USA*
[2]*Birck Nanotechnology Center, West Lafayette, Indiana 47907, USA*
[3]*School of Electrical and Computer Engineering, Purdue University, West Lafayette, Indiana 47907, USA*
[4]*Institute of Microwaves and Photonics, School of Electronic and Electrical Engineering, University of Leeds, Leeds LS2 9JT, United Kingdom*
[5]*School of Materials Engineering, Purdue University, West Lafayette, Indiana 47907, USA*
[6]*Center for Functional Nanomaterials, Brookhaven National Laboratory, Upton, New York, 11973, USA*

(Received 12 September 2013; revised manuscript received 11 November 2013; published 10 December 2013)

We report a systematic and quantitative study of near-infrared intersubband absorption in strained AlGaN/GaN and lattice-matched AlInN/GaN superlattices grown by plasma-assisted molecular-beam epitaxy as a function of Si-doping profile with and without δ doping. For AlGaN/GaN, we obtained good theoretical agreement with experimental measurements of transition energy, integrated absorbance and linewidth by considering many-body effects, interface roughness, and calculations of the transition lifetime that include dephasing. For the AlInN/GaN system, experimental measurements of the integrated absorbance due to the superlattice transitions produced values more than one order of magnitude lower than AlGaN/GaN heterostructures at similar doping levels. Furthermore, observed transition energies were roughly 150 meV higher than expected. The weak absorption and high transition energies measured in these structures is attributed to columnar alloy inhomogeneity in the AlInN barriers observed in high-angle annular dark-field scanning transmission electron microscopy. We simulated the effect of these inhomogeneities using three-dimensional band-structure calculations. The inhomogeneities were modeled as AlInN nanorods with radially varying In composition embedded in the barrier material of the superlattice. We show that inclusion of the nanorods leads to the depletion of the quantum wells (QWs) due to localization of charge carriers in high-In-containing regions. The higher energy of the intersubband transitions was attributed to the relatively uniform regions of the QWs surrounded by high Al (95%) composition barriers. The calculated transition energy assuming $Al_{0.95}In_{0.05}N$ barriers was in good agreement with experimental results.

DOI: 10.1103/PhysRevB.88.235306 PACS number(s): 78.67.De, 78.66.Fd

I. INTRODUCTION

III-nitride superlattices have attracted interest for near- and far-infrared (1.3 to 143 μm)[1–7] intersubband (ISB) devices due to the large available conduction band offset (>1 eV), and longitudinal-optical phonon energy (~90 meV). These devices include novel light detectors and emitters tunable by design in broad spectral regions that are relatively inaccessible to other material systems. However, there are still several challenges that impede progress towards the realization of high-performance infrared III-nitride devices. For example, the lattice mismatch between GaN and commonly used substrates, such as sapphire, results in a high defect density that hinders the vertical transport required for complex optoelectronic devices.[4] In addition to defects caused by the use of nonnative substrates, there are also strain-generated dislocations due to the lattice mismatch between the well and barrier materials. Most III-nitride ISB devices reported in the literature utilize AlGaN/GaN heterostructures for which there is no lattice-matched alloy composition.[1–4] Therefore, AlGaN is not the ideal material for the development of complex devices such as quantum cascade lasers (QCL) that often require active-region thicknesses on the order of microns.[8,9] However, exact in-plane lattice matching is possible for AlInN/GaN heterostructures at roughly 18% In composition.[5] We have already demonstrated ISB absorption in AlInN/GaN superlattices,[6,7] but growth of high-quality AlInN remains difficult to achieve. In addition to the challenges associated with material growth, heavy silicon doping is required ($>1\times10^{18}$ cm^{-3}) to measure ISB absorption in the III-nitrides. Large charge densities have both direct and indirect effects on transition energy and linewidth, and ultimately on device performance. The strong influence of many-body effects such as depolarization shift and exchange interaction on ISB transition energies at high charge densities has already been demonstrated in AlGaN/GaN superlattices,[1,2,10] while the location of δ doping in AlGaN/GaN heterostructures was found to have an indirect impact on structural quality and ISB linewidth.[11]

We present a comparative study of ISB absorption in high-quality AlGaN/GaN and near lattice-matched AlInN/GaN heterostructures grown by molecular-beam epitaxy (MBE) on low-defect GaN substrates. It has been previously shown that the number of defects in the heterostructures is drastically reduced by the use of thick GaN templates (50–100 μm) grown by hydride vapor phase epitaxy (HVPE) on sapphire,[12] and of commercially available freestanding GaN substrates,[13] The freestanding GaN substrates have dislocation densities of the order of 10^6 cm^{-2}, while GaN templates grown on sapphire substrates typically have dislocation densities $\sim10^8$ cm^{-2}. To further mitigate defect generation in thick nitride heterostructures, we also took advantage of the lattice matching between GaN and AlInN at roughly 18% In composition. For both lattice-matched AlInN/GaN and strained AlGaN/GaN heterostructures, the MBE growth process on the two types of low-defect substrates was optimized, and the material quality

was assessed with structural techniques and infrared optical spectroscopy. Various continuous and δ-doping schemes were considered. Here, δ doping is an attractive technique to significantly increase charge density when the maximum bulk doping density is limited by the available Si source. For AlGaN/GaN, we obtained good theoretical agreement with experimental measurements of transition energy, integrated absorbance, and linewidth by considering many-body effects, interface roughness, and calculations of the transition lifetime that include dephasing. For the AlInN/GaN system, experimental measurements of the integrated absorbance due to the superlattice transitions produced values more than one order of magnitude lower than AlGaN/GaN heterostructures at similar doping levels. Furthermore, observed transition energies were roughly 150 meV higher than expected. The weak absorption and high transition energies measured in these structures is attributed to columnar alloy inhomogeneity observed in high-angle annular dark-field scanning transmission electron microscopy (HAADF-STEM) images of AlInN. Atom probe tomography (APT) measurements carried out on bulk AlInN films by Choi *et al.*[14] found that these columnar inhomogeneities form a honeycomblike nanostructure. We modeled the effect of these inhomogeneities using three-dimensional (3D) band structure calculations. The inhomogeneities were considered as AlInN nanorods with radially varying In composition embedded in the barrier material of the superlattice. The dimensions and alloy composition of the nanorods is roughly based on APT measurements of Ref. 14. We show that inclusion of the nanorods leads to the depletion of the quantum wells (QWs) due to the localization of charge carriers in high In containing regions. Therefore, we attribute the weak absorption observed in AlInN/GaN superlattices to the compositional variations found in the honeycomb nanostructure. The high energy of the transitions was attributed to the relatively uniform regions of high-Al (95%) composition that surround the nanorods. The calculated energy assuming $Al_{0.95}In_{0.05}N$ barriers was in good agreement with experimental results.

II. MATERIAL GROWTH AND OPTICAL CHARACTERIZATION

A. MBE growth of AlInN/GaN and AlGaN/GaN heterostructures

The AlGaN/GaN superlattices were grown by molecular-beam epitaxy under Ga-rich conditions at 745 °C on low-defect *c*-plane freestanding GaN substrates from Kyma Technologies. A summary of the samples is given in Table I. The substrates were unintentionally doped for all but one sample that was grown on a semi-insulating substrate (sample B, see Table I). Nitrogen was supplied by a radio frequency plasma source with a power of 300 W and a flow rate of 0.5 standard cubic centimeters per minute at standard temperature and pressure (SCCM). Silicon was provided as an *n*-type dopant by a high-purity solid-source filament cell. To determine the optimal doping scheme, several continuous and δ-doping profiles were considered. The samples are structurally identical and differ only in the doping scheme. The 15-period AlGaN/GaN superlattices were characterized with high-resolution transmission electron microscopy (HRTEM) and high-resolution x-ray diffraction

TABLE I. Summary of the ISB absorption measurements (transition energy, FWHM, and integrated absorbance) for the samples investigated in this study. The location of the δ doping is given in parenthesis in monolayers (ML) from the beginning of growth of the QW. In the majority of samples, two transitions were observed. Transition 1 is attributed to the QW formed at the bulk-superlattice interface, while transition 2 is attributed to the superlattice QWs. PIA indicates result of photo-induced absorption measurements; Exp indicates experiment; and Calc indicates calculated.

Sample	Superlattice parameters (well/barrier ML)	Barrier material	Continuous doping (well/barrier cm^{-3})	δ doping (cm^{-2})	Transition 1 (Interface QW)					Transition 2 (Superlattice QWs)				
					Energy (meV)		Integrated Absorbance (meV)		FWHM (meV)	Energy (meV)		Integrated Absorbance (meV)		FWHM (meV)
					Exp	Calc	Exp	Calc	Exp	Exp	Calc	Exp	Calc	Exp
A	15 × 10/10	$Al_{0.70}Ga_{0.30}N$	3.8E19/-		380	347	33	3	220	616 (PIA)	610	–	11	226 (PIA)
B	15 × 10/10	$Al_{0.70}Ga_{0.30}N$	3.8E19/5.4E19		440	439	7	3	160	690	682	54	49	160
C	15 × 10/10	$Al_{0.70}Ga_{0.30}N$	3.8E19/-	2.7E14 (10 ML)		439		3		675	610	53	11	94
D	15 × 10/10	$Al_{0.70}Ga_{0.30}N$	3.8E19/5.4E19	2.7E14 (10 ML)		439		3		654	682	58	49	87
E-1	15 × 10/10	$Al_{0.70}Ga_{0.30}N$	3.8E19/5.4E19	2.7E14 (3 ML)	420	439	5	3	160	672	682	60	49	220
E-2	15 × 10/10	$Al_{0.70}Ga_{0.30}N$	3.8E19/5.4E19	2.7E14 (3 ML)		439		3		709	682	67	49	224
F	10 × 12/12	$Al_{0.85}In_{0.15}N$	5.3E19/1.2E20		310	426	60	4	110		525		30	110
G	20 × 14/10	$Al_{0.84}In_{0.16}N$	5.9E19/1.4E20	1.4E14 (7 ML)	303	418	52	4	116	680 (PIA)	494		75	150 (PIA)
H	20 × 14/10	$Al_{0.84}In_{0.16}N$	5.9E19/1.4E20	2.7E14 (7 ML)	308	418	31	4	136	665	494	6	75	211

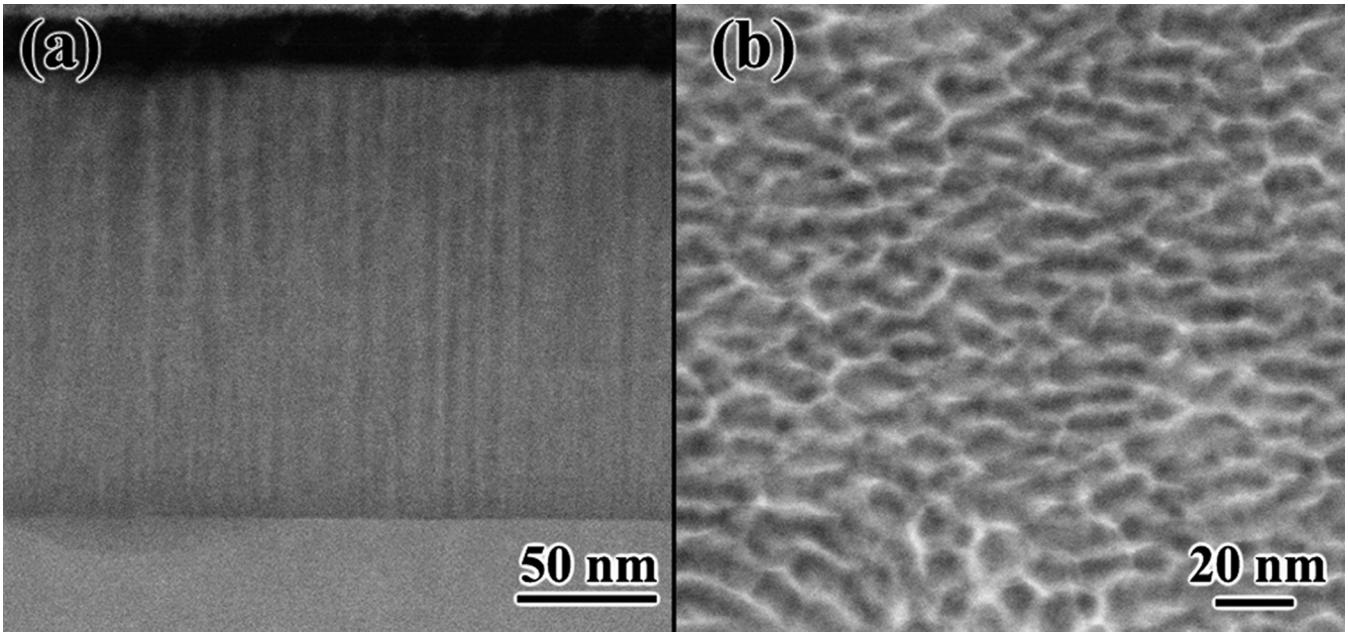

FIG. 1. (a) Cross-sectional and (b) plan-view HAADF-STEM images of a 175-nm $Al_{0.85}In_{0.15}N$ film. Bright regions correspond to higher In composition.

(HRXRD). Theoretical simulation of the x-ray diffraction pattern using the commercial software package Panalytical X'PERT EPITAXY combined with HRTEM imaging allow for the determination of the well and barrier thicknesses as well as the Al composition. Silicon-doping levels were calibrated using secondary ion mass spectrometry (SIMS). The bulk impurity density for GaN was measured to be 3.8×10^{19} cm^{-3}. Doping density for AlGaN was estimated by assuming the Si incorporation rate in GaN obtained by SIMS and adjusting for the difference in growth rates. To further increase charge density, δ doping was deposited in several samples during a growth pause of 5 min at the location indicated in Table I, i.e. either close to the middle of the QW [3 monolayers (ML)] or after the deposition of the QW (10 ML). During this pause the Ga, Al, and plasma shutters were closed.

The growth of AlInN films requires a different approach to that of typical AlGaN MBE growth.[15] While high-quality AlN growth occurs at high temperature, indium is only incorporated at lower temperatures. Therefore, in order to achieve sufficient indium composition for lattice-matched AlInN films, we have chosen a lower growth temperature of 530 °C. Optimum growth conditions were obtained at a total metal flux of 9.5×10^{-8} Torr and an In/Al flux ratio of ~0.8.[6] This resulted in a growth rate of 3.3 nm/min for AlInN. Transmission electron microscopy measurements carried out on a cross-section of a 175-nm $Al_{0.85}In_{0.15}N$ layer grown under these conditions indicate that no threading dislocations were generated in this thick layer. However, bright stripes along the growth direction were visible under HAADF-STEM [Fig. 1(a)], suggesting that the alloy composition is laterally inhomogeneous on the scale of a few nanometers. These compositional inhomogeneities have been widely reported in the literature[14,16–18] and are attributed to the large lattice mismatch (13%) between AlN and InN. In the cross-sectional image, the bright (high-In containing) regions can be seen to form columns propagating along the growth direction, while the plan-view images reveal that these columns form a honeycomb nanostructure [Fig. 1(b)]. The exact compositional variation of this nanostructure has been characterized in detail with ATP.[14] Large in-plane variation of the In composition (5–40%) was observed with the highest In composition occurring at the meeting points of the honeycomb walls. The area circumscribed by the walls is relatively uniform with an In content of only 5%.

Using the growth parameters discussed above, AlInN/GaN heterostructures were grown. To investigate the impact of doping level on ISB absorption in AlInN/GaN, the δ-doping density was varied across three samples (F-H) by increasing the duration of the growth interruption. As for AlGaN, the doping density for AlInN was estimated by assuming the GaN incorporation rate obtained by SIMS and adjusting for the difference in growth rates. The superlattice parameters were characterized with HAADF-STEM and HRXRD. Based on this analysis, the superlattice parameters and average In composition were determined for each sample (see Table I). The average In composition measured by HRXRD was between 15–16% for all samples, close to the lattice-matched composition of 18%. However, similar columnar inhomogeneities are observed along the growth direction in the AlInN barrier (Fig. 2). We investigated the impact of these columnar inhomogeneities on intersubband absorption using 3D band structure calculations. The results are discussed in Sec. IVC.

B. Optical characterization of ISB transitions

The optical properties of the samples were characterized using Fourier-transform infrared (FT-IR) spectroscopy on samples polished into 45° multipass waveguides. Both direct and photo-induced absorption (PIA) measurements were carried out. In both measurements, a polarizer was used to isolate the

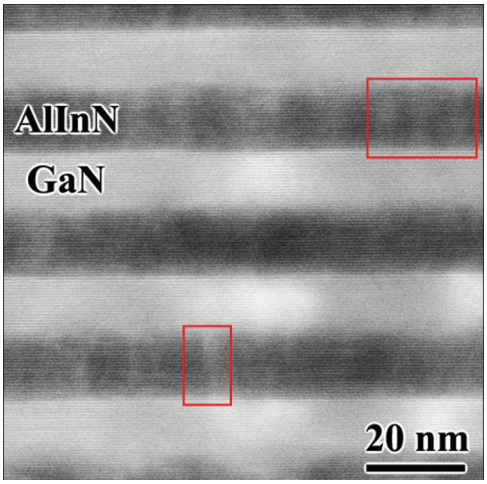

FIG. 2. (Color online) HAADF-STEM images of a AlInN/GaN superlattice with 12-nm wells and 13-nm barriers. Bright columns attributed to the In nanostructure appear in the AlInN barrier. Red boxes are used to highlight several columns for illustration.

ISB transitions. For PIA, an optically chopped 15-mW HeCd laser operating at 325 nm was used to modulate the electron density, and the differential transmission was measured in step-scan mode using a lock-in amplifier. All spectra display the normalized absorbance $A(\omega)$, which can be obtained from transmission spectra via the relation:

$$T(\omega) = \exp[-A(\omega) \cdot C \cdot M \cdot \sin^2\theta/\cos\theta], \tag{1}$$

where M represents the number of passes through the active region, θ is the angle between the radiation propagation vector and growth direction, and C is an electric-field coupling factor between 0 and 2, which represents the overlap of the electric field with the active region. The electric-field overlap was estimated by calculating the average value of the electric field over the active region at the peak absorption wavelength, assuming a node at the air-semiconductor interface. In some cases, the absorption was attributed to the triangular well formed at the bulk-superlattice interface. In these cases, the electric-field overlap was taken to be equal to the magnitude of the field at this interface. Since the normalization must be different for each transition, the spectra displayed here are normalized using the coupling factor for the dominant transition in that sample, while the integrated absorbance values reported for each transition in Table I use the appropriate coupling coefficient.

III. THEORETICAL BACKGROUND

A. Band-structure calculations

In this paper, the band structures of the AlGaN/GaN and AlInN/GaN superlattices were calculated self-consistently using the eight-band $\mathbf{k}\cdot\mathbf{p}$ model with the nextnano3 software.[19] Many-body effects were included according to the method presented in Ref. 1 (see Supplemental Materials[20]). The material parameters used in the calculation are summarized in Ref. 21. The appropriate bowing parameters for both AlGaN and AlInN were used when available. Otherwise, a linear interpolation was assumed. For GaN, Si doping is considered to be thermally ionized, and an activation energy of 30 meV is used. Doping in the barrier is expected to be fully ionized since the activation energy of Al-containing nitrides has been shown to be small compared to the large conduction band offset.[22]

The theoretical value of the integrated absorbance for each sample was determined by integrating over $A(\omega)$, which was calculated according to the following equation:

$$A(\omega) = \frac{e^2\tilde{\omega}_{ij}^2}{2\pi\varepsilon_0 cn\omega}|\langle i|z|j\rangle|^2 \times \int_0^\infty L(\hbar\omega,\hbar\tilde{\omega}_{ij},k^2)F_{ij}(k^2)d^2k, \tag{2}$$

where n is the refractive index, c the velocity of light, ε_0 is the vacuum permittivity, z is the position operator, and $\hbar\omega$ and $\hbar\tilde{\omega}_{ij}$ are the photon and peak absorption energies, respectively. Here, F_{ij} is the difference of Fermi-Dirac factors for the two states, and L is the normalized Lorentzian:

$$L(\hbar\omega,\hbar\tilde{\omega}_{ij},k^2) = \frac{\Gamma/2\pi}{(\hbar\omega - \hbar\tilde{\omega}_{ij})^2 + (\Gamma/2)^2}, \tag{3}$$

where Γ is the full width at half maximum (FWHM) broadening of the ISB transition.

B. Scattering calculations

The linewidth Γ is an important parameter in the operation of ISB devices such as quantum cascade lasers and has several important contributions, including scattering due to phonons, electron-electron interactions, ionized impurities, alloy disorder, and interface roughness. The contribution of interface roughness to the linewidth is due to both long- and short-range roughness. Long-range roughness broadening arises from a spread of transition energies due to variation of the QW width, while short-range roughness must be considered as a perturbing potential. In this paper, only long-range roughness was considered. Its contribution to the linewidth was determined by averaging the calculated absorbance curves for various QW widths weighted by the thickness distribution obtained from HRTEM analysis as in Ref. 11.

The theoretical linewidth contributions due the other scattering processes were calculated as in Refs. 23 and 24. The effect of dephasing on the broadening was included by summing over the intrasubband scattering rates. In the case of electron-electron scattering, we consider only the effect of intersubband scattering lifetimes as a first approximation since nonparabolicity is neglected in our scattering calculations.[25] Due to the large doping densities in the samples considered in this study, impurity scattering is expected to contribute significantly to the broadening. We account for the screening of impurity charge by local carriers with an inverse screening length correction to the scattering wave vector.

IV. EXPERIMENTAL RESULTS AND DISCUSSION

A. Quantitative analysis of intersubband absorption properties of AlGaN/GaN superlattices

To determine the effect of doping profile on the ISB absorption properties of AlGaN/GaN heterostructures, the absorbance spectra were characterized by FT-IR spectroscopy.

The transition energy, FWHM, and integrated absorbance for each sample is shown in Table I. In some cases, two peaks are observed. The low-energy peak (<450 meV) is attributed to the triangular well formed by the polarization discontinuity at the bulk-superlattice interface, while the high-energy peak (>600 meV) is attributed to the superlattice. For the sample doped only in the well (sample A), the absorption spectrum is dominated by the low-energy transition (380 meV) [Fig. S2(a) in the Supplemental Material[20]]. The high-energy peak attributed to the superlattice was only observed in PIA measurements. The dominance of the interface well at lower doping levels can be explained by depletion of the superlattice due to Fermi-level pinning at the AlGaN cap layer[11] (see Supplemental Material[20]). For samples doped both in the well and barrier (samples B through E), the spectra are dominated by the higher-energy peak (>600 meV) attributed to the superlattice. The transition energies for the interface and superlattice transitions were calculated according to the method presented in Sec. IIIA. Agreement was achieved to within 10% (see Table I). To verify the accuracy of the band structure and many-body calculations, Hall effect measurements were carried out on sample B, which was grown on a semi-insulating substrate. A sheet density of 2.29×10^{14} cm^{-2} was obtained, in agreement with the total sheet density of 2.49×10^{14} cm^{-2} calculated from band structure simulations based on the nominal doping level.

To investigate the strength of the interface and superlattice intersubband transitions, the theoretical integrated absorbance for each doping configuration was calculated and compared to experimental values obtained from fits of the normalized absorbance spectra (see Table I). For samples dominated by the superlattice transition (B through E), the integrated absorbance was found to vary from 53 to 67 meV. The predicted integrated absorbance for samples doped only in the well is 11 meV. Addition of doping in the barrier increases the expected absorbance to 49 meV. The large difference is due to the decreased effective activation energy of barrier dopants associated with the higher potential of this region. This leads to full ionization of the barrier dopants, while well dopants are only partially ionized. Since barrier doping is the dominant contribution to the charge density, the addition of δ doping in the well did not lead to increased absorbance in our simulations. The predicted value of 49 meV is in reasonable agreement with the observed values for these samples, especially for sample B, for which the sheet density measured by Hall effect was found to be in good agreement with theoretical predictions. However, all samples displayed somewhat higher integrated absorbance than expected (up to 67 meV for sample E-2). These larger experimental values may be due to spread of the well doping into the barrier, where increased activation is expected. Our simulations assume the δ doping is placed at a single point in the well and therefore is largely un-ionized compared to the barrier doping. However, in practice, the δ-doping distribution will have a finite width. This effect is especially apparent for sample C, which was not doped in the barrier but shows an integrated absorbance comparable to the other samples.

The integrated absorbance of sample A was much larger than expected. The transition due to the interface well is predicted to have an integrated absorbance of only 3 meV, compared to the experimental value of 33 meV. The inability of our calculations to reproduce the magnitude of this transition may be due to the our limited approach to the many-body calculations, which assumes that these effects are small relative to the bare transition energy and that only the ground subband is occupied. Before any corrections, the calculated transition energy for the interface transition is roughly 200 meV. Inclusion of many-body effects as outlined in Sec. IIIA, leads to a final energy as high as 439 meV. Since the energy correction is roughly equal to the bare energy, it is unclear that a perturbative approach is adequate. Furthermore, our calculations predict significant occupation of multiple subbands in the triangular well. For the doping levels considered in this paper, the sheet density for the second and third subband is expected to reach the mid-10^{12} and -10^{11} cm^{-2} range, respectively. Under such conditions, considerable enhancement of the intersubband absorption has been observed in the GaInAs/AlInAs material system and was attributed to the formation of a multisubband plasmon coupled by the Coulomb interaction.[26]

B. Broadening of intersubband transitions in AlGaN/GaN superlattices

We have previously reported that the absorption lineshape shows a strong dependence on the δ-doping position.[11] For the samples δ doped at the end of the well (C and D), a full width at half maximum (FWHM) of roughly 90 meV was obtained. This result is comparable to typical FWHM values reported in the literature for doped superlattices.[2] Other doping schemes resulted in FWHM values of at least 160 meV. The smaller FWHM of the well edge δ-doped samples has been attributed to a decrease in interface roughness observed in the HRTEM images.[11] The reduction in roughness is associated with the growth interruption at the GaN/AlGaN interface needed for Si-atom accumulation. During this 5-min pause, excess Ga atoms are consumed, leaving behind a smooth surface for AlGaN growth that improves the overall quality of the superlattice. Moreover, we have shown that the impact of interface roughness can be modeled by averaging the calculated absorbance curves for various QW widths weighted by the thickness distribution obtained from HRTEM analysis.[11] Figure 3 compares the experimental absorption

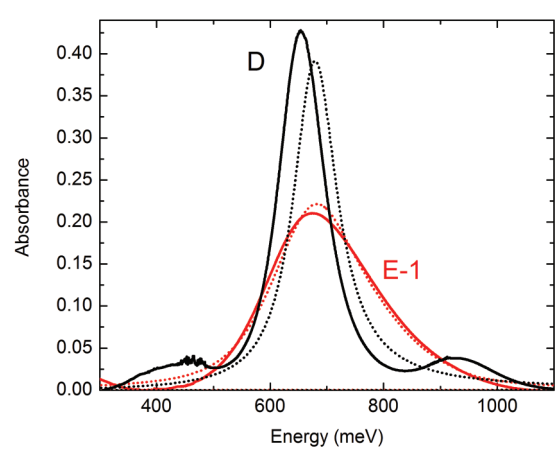

FIG. 3. (Color online) Experimental (solid) and theoretical (dashed) absorbance spectra for samples D (black) and E-1 (red).

TABLE II. Homogenous contributions to transition linewidth from impurity scattering calculated with Thomas-Fermi screening, e-e = electron-electron scattering, e-LO = longitudinal-optical phonon scattering, e-AP = acoustic phonon scattering.

Scattering mechanism	Impurity (meV)	e-e (meV)	Alloy disorder (meV)	e-LO (meV)	e-AP (meV)	Total (meV)
Broadening contribution	99	0.10	0.20	2.5	0.10	102

with the theoretical absorption calculated using a homogenous broadening of 90 meV (based on our narrowest measured linewidth) and the interface roughness estimated from HRTEM measurements (see Fig. S3 in the Supplemental Material[20]) for a well edge and well-center δ-doped sample. We emphasize that all properties of the experimental intersubband absorption features (energy, linewidth, and integrated absorption) are accurately reproduced by our model.

To assess the accuracy of the value for homogeneous broadening, scattering rate calculations were carried out according to the method presented in Sec. IIIB. Unlike in previous reports,[27] we find the impurity scattering to be the dominant scattering mechanism. This difference is largely due to the higher doping levels considered in this paper. The strong internal electric fields cause significant penetration of the first excited state wave function into the barriers, where the dopants are fully ionized. Therefore, intrasubband scattering within the excited state by impurities is the primary contribution to the overall lifetime. The effect of impurities on the broadening is highly dependent on the screening length implemented. Without correcting for the screening of the ionized dopants, the linewidth predicted would be extremely large (roughly 8 eV). For the well edge δ-doped samples, the Thomas-Fermi screening results in a linewidth contribution of 99 meV to lifetime broadening, compared to only 33 meV for Debye screening. The relative importance of the other scattering mechanisms is shown in Table II. Given the small scale of the contributions from alloy disorder and phonon scattering, it is clear that only Thomas-Fermi screening is consistent with producing enough broadening in impurity scattering to match experimental values. The total broadening calculated by this method is 102 meV, in good agreement with the experimental measurement of the broadening for samples δ doped at the end of the well. We emphasize that agreement with experimental data is achieved only when the effect of dephasing is included, which contributes to the broadening as the sum of the intrasubband scattering rates. Repeating the calculation above for the well-center δ-doped samples (e.g. sample E-1) yields the same result because the δ doping is not expected to be ionized (see Sec. IVA). This indicates that the remaining contribution to the broadening for samples with larger FWHMs has been correctly attributed to interface roughness in our previous work.[11]

C. Intersubband absorption in AlInN/GaN heterostructures

The optical properties AlInN/GaN heterostructures with various doping schemes were determined and compared to the AlGaN/GaN results. The well and barrier thicknesses used for AlInN/GaN and AlGaN/GaN were kept the same within a few monolayers (see Table I). The continuous doping level in the well was similar. However, doping in the barrier is increased by roughly a factor of two due to the slower growth rate of AlInN. All AlInN/GaN samples were doped in the well and barrier at the same level, while the δ-doping density was varied. Sample G was grown without δ doping. The resulting absorption spectrum (Fig. 4) shows a low-energy peak at 310 meV. Additional PIA measurements were carried out on this sample, but no other features were observed. Low-energy peaks were also measured in some AlGaN samples (e.g. sample A). These peaks have been attributed to the triangular QW formed by the polarization fields at the bulk-superlattice interface and were found to dominate the spectrum at lower doping levels.[11] The integrated absorption of 60 meV is much larger than the calculated value of 4 meV. However, the large magnitude of this integrated absorption is consistent with larger-than-expected values obtained in AlGaN/GaN measurements (Sec. IVA). For AlGaN/GaN, we suggested the enhanced absorption could be due to multisubband plasmon resonances formed due to the occupation of the higher subbands.[26] The calculated energy for this transition is 462 meV, roughly 150 meV higher than the experimental value. As was the case for AlGaN/GaN, the many-body correction is roughly equal to the bare transition energy. Therefore, the discrepancy between the calculated and observed transition energies is likely due to the inadequacy of the perturbative approach.

Samples G and H were δ doped at the center of the well with densities of 1.4×10^{14} and 2.7×10^{14} cm^{-2}, respectively (see Table I). For both samples, the lower-energy transition was observed in direct measurements (Fig. 4). For sample G, the higher-energy absorption attributed to the superlattice was observed in PIA measurements at 680 meV but was too weak to be observed in direct absorption (Fig. 4 inset). This result is in contrast to theoretical predictions and the previous

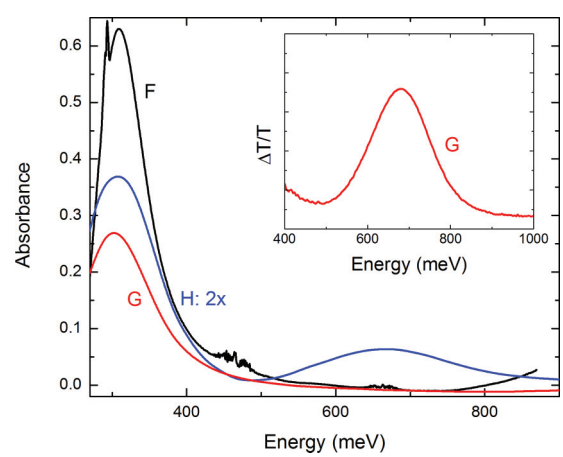

FIG. 4. (Color online) Absorbance for samples F, G, and H. For viewing purposes, absorbance of sample H has been magnified by factor of 2. Inset shows PIA spectrum for sample G.

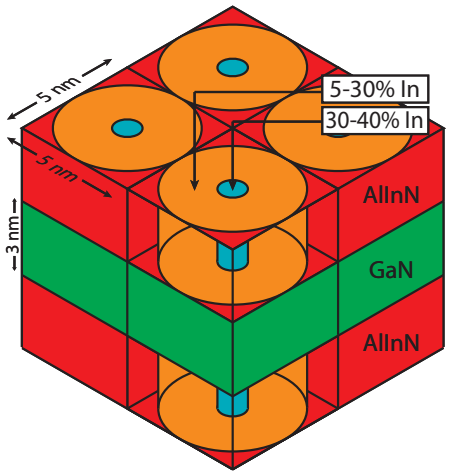

FIG. 5. (Color online) Schematic of the 3-nm AlInN/3-nm GaN superlattice with AlInN nanorods embedded in the barrier material. The nanorods lie along the growth direction embedded in an $Al_{0.95}In_{0.05}N$ layer and are distributed in a 5×5 nm^2 periodic array. The composition of the nanorod varies from 40 to 5% In from center to edge.

AlGaN/GaN results, where the superlattice transitions were already observed in direct absorption at lower doping levels. Due to the higher doping level in the AlInN barrier, the expected integrated absorbance for this sample was 75 meV, larger than values for similarly doped AlGaN/GaN samples (e.g. 49 meV for sample E). Sample H displayed absorption in direct absorption measurements at an energy of 665 meV (Fig. 4). This result is in contrast to theoretical predictions since calculations do not predict an increase in integrated absorbance with increased δ doping due to the relatively high activation energy of donors located in the QW. As was suggested for the AlGaN/GaN samples, however, the increased absorbance relative to sample G may be due to partial diffusion of δ dopants into the barrier. Despite the increase in absorption, the normalized integrated absorbance of the high-energy transition was measured to be only 6 meV, more than a factor of 10 times lower than theoretical predictions. These results are in contrast to those on AlGaN/GaN superlattices where reasonable agreement with experimental measurements of the integrated absorbance was obtained. The FWHMs of 150 and 211 meV were measured for samples G and H, respectively. The increase from sample G to H is likely due to a factor of two increase in δ doping since impurity scattering was found to be the dominant contribution to the ISB lifetime for AlGaN/GaN superlattices. Calculations of ISB transition energy utilizing the eight-band $\mathbf{k}\cdot\mathbf{p}$ model and many-body corrections produce theoretical transition energies of 494 meV for both samples, significantly lower than the experimental values of 680 and 665 meV for samples G and H, respectively. Furthermore, although the higher energy of these transitions indicates that the addition of δ doping has shifted the charge density into the superlattice, consistent with AlGaN/GaN measurements, the integrated absorbance due to the superlattice transition remained small.

D. Effect of alloy inhomogeneities on ISB absorption in AlInN/GaN heterostructures

To explain the weak absorption and high energies observed in AlInN/GaN heterostructures, we have carried out 3D band structure calculations that simulate the effects of the honeycomb nanostructure observed in HAADF-STEM images of our AlInN films. Since the largest inhomogeneities occur in the columns formed at the intersection of the hexagonal walls (up to 40% In), our simulations focus on the effect of these regions. The nanostructure is simulated with a simplified model of a single AlInN nanorod with radially varying composition embedded in the barrier material of the heterostructure. A schematic of the simulation domain is shown in Fig. 5. The dimensions and alloy composition of the nanorods are roughly based on the compositional maps obtained by ATP in Ref. 14. The nanorods have a radius of 5 nm, while the alloy

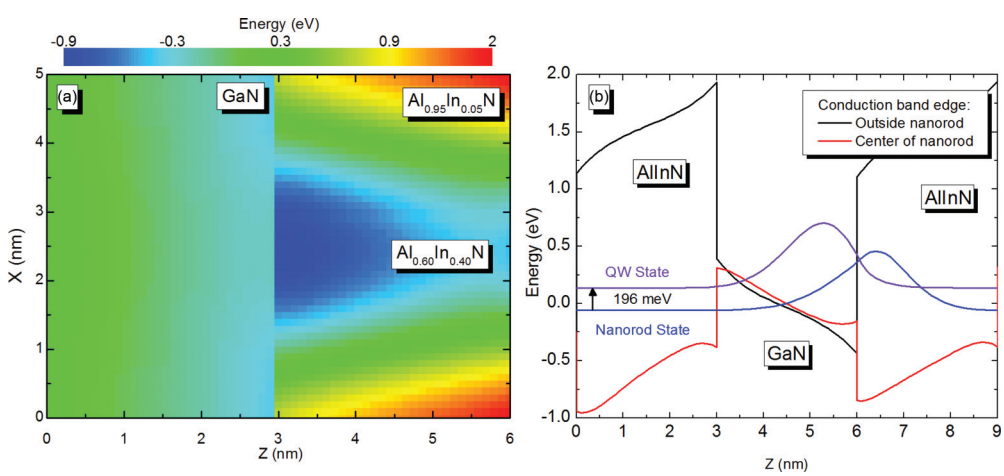

FIG. 6. (Color online) (a) 2D and (b) 1D slices of the conduction band profile for the AlInN/GaN heterostructure modeled with the nanorod structure shown in Fig. 8. The 2D slice is taken at the center of the nanorod in the x-z plane, while the 1D slices are along the z direction both outside and at the center of the nanorod. Wave functions in (b) have been integrated over the x-y plane to show the distribution along the z direction. The ground state of the system is located in the nanorod (blue curve), while the lowest energy state localized outside the nanorod (purple curve labelled as QW state) is approximately 192 meV higher.

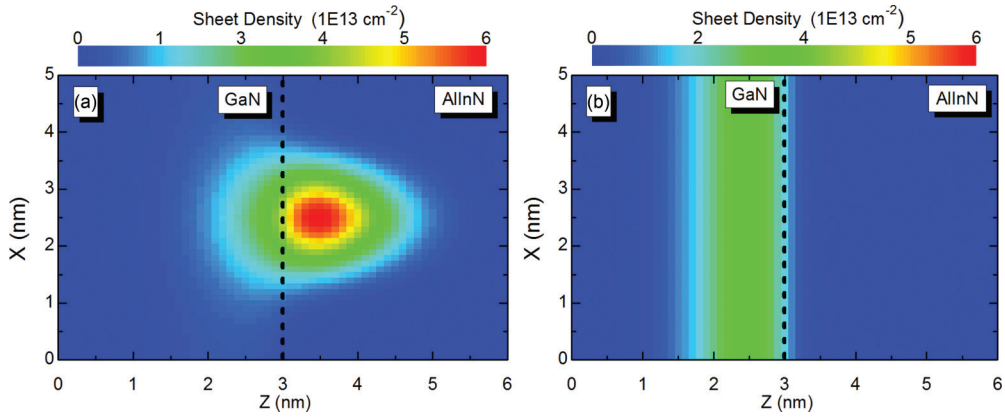

FIG. 7. (Color online) 2D sheet density in the AlInN/GaN superlattice in the (x-z) plane (a) with and (b) without the nanorod. Note that with the addition of the nanorod, the charge density becomes localized in the barrier, depleting the QW.

inhomogeneities are described by a Gaussian distribution that varies from 40% to 5% In composition from center to edge. The rods lie in a background of 5% In composition AlInN and are distributed in a 5×5 nm^2 periodic array in the (x-y) plane. Along the (z) growth direction, we consider a superlattice with well and barrier thicknesses of 3 nm, resulting in an overall periodicity of 6 nm. The well is doped with a concentration of 7×10^{19} cm^{-3}.

The band structure calculations were done using the single-band approximation with material parameters obtained from Ref. 21. The large bandgap bowing parameter of AlInN is essential to obtain reasonable conduction band offsets since In composition approaches 50%. The impact of bowing was considered to only affect the conduction band edge, while the valence band offset was solely determined by a linear interpolation of the values for AlN and InN. This assumption produced conduction band offsets in agreement with Ref. 28 to within experimental error, where the offset was determined at In compositions from 17 to 30%. The conduction band offset decreased from 1.54 to -0.69 eV as the In composition increased from 5 to 40%. Figure 6(a) shows a two-dimensional (2D) slice of the band diagram at the center of the nanorod, while Fig. 6(b) shows one-dimensional (1D) slices along the z direction both outside and at the center of the nanorod. Note that the lowest potential occurs inside the nanorod at the region of highest In composition (40%) rather than in the QW. The low potential of this region results in a localized ground state with energy approximately 200 meV below the states localized in the QW [Fig. 6(b)].

The band structure shown in Figs. 6(a) and 6(b) has a dramatic effect on the charge distribution in the superlattice. The resulting sheet density is plotted in Fig. 7(a) for a well doping level of 7×10^{19} cm^{-3}. Note that, at this doping level, the majority of the carriers are concentrated in the nanorod, while the QW remains relatively depleted throughout the simulation volume. For comparison, the sheet density for a simple $Al_{0.95}In_{0.05}N$/GaN quantum well without the nanorod is shown in Fig. 7(b). We note that the triangular QW at the bulk-heterostructure interface experiences less depletion due to the lower energy of the ground state. This explains the observation of the low-energy peak (310 meV) even at the lowest doping level.

We attribute the weak near-infrared intersubband absorption of AlInN/GaN superlattices to the depletion of the charge from the QWs by the columnar compositional inhomogeneities in the AlInN barriers. The level of depletion will depend on the doping level, alloy composition, and density of nanorods, and therefore ultimately on the material growth conditions. For the structure modeled here, the QWs are nearly completely depleted as shown in Fig. 7(a), and no intersubband absorption from the superlattice is expected, as was observed in both direct and PIA measurements of sample F. With increasing doping density, the Fermi level increases, and significant occupation of the QWs away from the nanorod-depleted regions occurs. This explains the observation of direct absorption in only the most highly doped sample (i.e. sample H). Sample G represents an intermediate doping case, in which the Fermi level is too low to observe direct absorption, but where the photoexcited carriers generated in the PIA measurement can increase the Fermi level enough to produce measureable absorption.

To explain the relatively high transition energies observed across samples, we emphasize that the uniform regions surrounding the nanorods are of high Al (95%) composition.

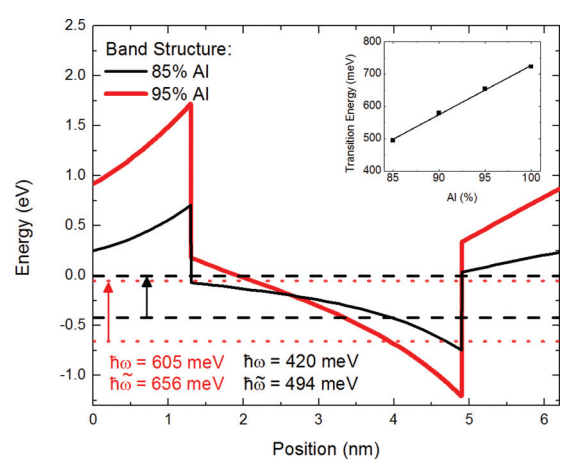

FIG. 8. (Color online) Band structure and energy levels for AlInN/GaN superlattices with 95% and 85% Al composition barriers. Inset shows the dependence of the transition energy on Al composition. Here, $\hbar\omega$ and $\hbar\tilde{\omega}$ are the bare and corrected transition energies, respectively (see Supplemental Materials[20]).

Due to the uniformity of these regions, they are expected to dominate the intersubband spectrum. We note that there may be transitions associated with the nanorod regions, but these structures are highly nonuniform (see Ref. 14), and therefore any spectral features associated with them may be too broad to observe. Figure 8 shows band structure calculations using the eight-band **k·p** model for AlInN/GaN heterostructures with varying barrier composition. The inset shows the dependence of the transition energy on Al content. As expected, higher Al content results in an increased transition energy due to the larger polarization field and conduction band offset. The calculated energy for these samples assuming $Al_{0.95}In_{0.05}N$ barriers and nominal doping is 656 meV, in good agreement with the experimental values of 680 and 665 meV for samples G and H, respectively.

V. CONCLUSIONS

In summary, we have investigated the effect of doping profile on the near-infrared ISB absorption line profile of AlGaN/GaN and AlInN/GaN superlattices. For both material systems, smaller doping concentrations resulted in spectra dominated by low-energy ISB transitions attributed to the triangular well formed at the bulk-superlattice interface. As the doping concentration increased, the relative intensity of the higher-energy transitions attributed to the superlattice increased. This trend may be explained by the reduction of the depletion region caused by Fermi-level pinning at the surface. However, we note that the magnitude of the absorption in the interface well was much stronger than expected. The strength of this transition may be related to occupancy of excited states, which can lead to the formation of a multisubband plasmon.[26] This effect is not included in our perturbative approach to the many-body corrections.

For AlGaN/GaN, we obtained good theoretical agreement with experimental measurements of transition energy, integrated absorbance, and linewidth by considering many-body effects, interface roughness, and calculations of the broadening that include dephasing. In AlInN/GaN superlattices, higher doping levels were required to produce measurable absorption from the superlattice. The integrated absorbance values for these transitions were more than one order of magnitude lower than AlGaN/GaN results at similar doping levels. Furthermore, observed transition energies were roughly 150 meV higher than expected. The weak absorption and high transition energies measured in these structures is attributed to columnar alloy inhomogeneities observed in HAADF-STEM. We modeled the effect of these inhomogeneities using 3D band structure calculations. The inhomogeneities were considered as AlInN nanorods with radially varying In composition embedded in the barrier material of the superlattice. The spacing and alloy composition of the rods were roughly based on APT measurements.[14] We show that inclusion of the nanorod leads to the depletion of the QWs due to the localization of charge carriers in high-In-containing regions. Therefore, we attribute the weak absorption observed in AlInN/GaN superlattices to the compositional variations found in the honeycomb nanostructure. The high energy of the measured superlattice transitions was attributed to the relatively uniform high-Al (95%) regions surrounding the nanorods. The calculated energy assuming $Al_{0.95}In_{0.05}N$ barriers was in good agreement with experimental results.

ACKNOWLEDGMENTS

This work was supported by the NSF awards ECCS-1001431, ECCS-1253720, and DMR-1206919; the Defense Advanced Research Project Agency (DARPA) under Contract No. D11PC20027; and the Univ. Leeds FIRC 2011 grant.

*Corresponding author: omalis@purdue.edu

[1] M. Tchernycheva, L. Nevou, L. Doyennette, F. H. Julien, E. Warde, F. Guillot, E. Monroy, E. Bellet-Amalric, T. Remmele, and M. Albrecht, Phys. Rev. B **73**, 125347 (2006).

[2] P. K. Kandaswamy, F. Guillot, E. Bellet-Amalric, E. Monroy, L. Nevou, M. Techernycheva, A. Michon, F. H. Julien, E. Baumann, F. R. Giogetta, D. Hofstetter, T. Remmele, M. Albrect, S. Birner, and Le Si Dang, J. Appl. Phys. **104**, 093501 (2008).

[3] H. Machhadani, Y. Kotsar, S. Sakr, M. Tchernycheva, R. Colombelli, J. Mageney, E. Bellet-Amalric, E. Sarigiannidou, E. Monroy, and F. H. Julien, Appl. Phys. Lett. **97**, 191101 (2010).

[4] D. Li, L. Tang, C. Edmunds, J. Shao, G. Gardner, M. J. Manfra, and O. Malis, Appl. Phys. Lett. **100**, 252105 (2012).

[5] S. Nicolay, J. F. Carlin, E. Feltin, R. Butté, M. Mosca, N. Grandjean, M. Ilegems, M. Tchermycheva, L. Nevou, and F. H. Julien, Appl. Phys. Lett. **87**, 111106 (2005).

[6] C. Edmunds, L. Tang, D. Li, M. Cervantes, G. Gardner, T. Paskova, M. J. Manfra, and O. Malis, J. Electr. Mat. **41**, 881 (2012).

[7] O. Malis, C. Edmunds, M. J. Manfra, and D. L. Sivco, Appl. Phys. Lett. **94**, 161111 (2009).

[8] E. Bellotti, K. Driscoll, T. D. Moustakas, and R. Paiella, Appl. Phys. Lett. **92**, 101112 (2008).

[9] E. Bellotti, K. Driscoll, T. D. Moustakas, and R. Paiella, J. Appl. Phys. **105**, 113103 (2009).

[10] P. K. Kandaswamy, H. Machhadani, Y. Kotsar, S. Sakr, A. Das, M. Tchernycheva, L. Rapenne, E. Sarigiannidou, F. H. Julien, and E. Monroy, Appl. Phys. Lett. **96**, 141903 (2010).

[11] C. Edmunds, L. Tang, J. Shao, D. Li, M. Cervantes, G. Gardner, D. N. Zakharov, M. J. Manfra, and O. Malis, Appl. Phys. Lett. **101**, 102104 (2012).

[12] R. J. Molnar, W. Götz, L. T. Romano, and N. M. Johnson, J. Cryst. Growth **178**, 147 (1997).

[13] T. Paskova, D. A. Hanser, and K. R. Evans, Proc. of the IEEE **98**, 1324 (2010).

[14] S. Choi, F. Wu, R. Shivaraman, E. C. Young, and H. S. Speck, Appl. Phys. Lett. **100**, 232102 (2012).

[15] S. Schmult, T. Siegrist, A. M. Sergent, M. J. Manfra, and R. J. Molnar, Appl. Phys. Lett. **90**, 021922 (2007).

[16] S. L. Sahonta, G. P. Dimitrakopulos, T. Kehagias, J. Kioseoglou, A. Adikimenakis, E. Iliopoulos, A. Georgakilas, H. Kirmse,

W. Neumann, and P. Komninou, Appl. Phys. Lett. **95**, 021913 (2009).

[17]L. Zhou, D. J. Smith, M. R. McCartney, D. S. Katzer, and D. F. Storm, Appl. Phys. Lett. **90**, 081917 (2007).

[18]S. Zhang, B. Liu, J. Y. Yin, H. H. Sun, Z. H. Feng, and L. C. Zhao, J. Phys. D: Appl. Phys. **44**, 075405 (2011).

[19]S. Birner, T. Zibold, T. Andlauer, T. Kubis, M. Sabathil, A. Trellakis, and P. Vogl, IEEE Trans. Electron Devices **54**, 2137 (2007).

[20]See Supplemental Material at http://link.aps.org/supplemental/10.1103/PhysRevB.88.235306 for details regarding many-body calculations, effect of Fermi-level pinning on the band structure, and determination of interface roughness from HRTEM analysis.

[21]J. Wu, J. Appl. Phys. **106**, 011101 (2009).

[22]R. Collazo, S. Mita, J. Xie, A. Rice, J. Tweedie, R. Dalmau, and Z. Sitar, Phys. Stat. Sol. C **8**, 2031 (2011).

[23]J. H. Davies *The Physics of Low-Dimensional Semiconductors* (Cambridge University Press, Cambridge, 1998).

[24]T. Unuma, M. Yoshita, T. Noda, H. Sakaki, and H. Akiyama, J. Appl. Phys. **93**, 1586 (2003).

[25]G. G. Zegrya and V. E. Perlin, Semiconductors **32**, 417 (1998).

[26]A. Deteil, A. Vasanelli, Y. Todorov, C. Feuillet Palma, M. Renaudat St-Jean, G. Beaudoin, I. Sagnes, and C. Sirtori, Phys. Rev. Lett. **109**, 246808 (2012).

[27]N. Suzuki and N. Iizuka, Jpn. J. Appl. Phys. **37**, L369 (1998).

[28]M. Akazawa, B. Gao, T. Hashizume, M. Hiroki, S. Yamahata, and N. Shigekawa, J. Appl. Phys. **109**, 013703 (2011).